Design and optimization of a high-speed, high-sensitivity, spinning disk confocal microscopy system

Ryan G. McAllister
Daniel R. Sisan
Jeffrey S. Urbach
Georgetown University
Department of Physics
Washington, DC 20057

Abstract. We describe the principles, design, and systems integration of a flexible, high-speed, high-sensitivity, high-resolution confocal spinning disk microscopy (SDCM) system. We present several artifacts unique to high-speed SDCM along with techniques to minimize them. We show example experimental results from a specific implementation capable of generating 3-D image stacks containing 30 2-D slices at 30 stacks per second. This implementation also includes optics for differential interference contrast (DIC), phase, and bright-field imaging, as well as an optical trap with sensitive force and position measurement. © *2008 Society of Photo-Optical Instrumentation Engineers.* [DOI: 10.1117/1.2992141]

1 Introduction

Understanding in all fields of cell biology benefits from optical imaging of dynamic subcellular processes.[1–3] Recent advances in imaging technology, combined with powerful techniques for fluorescent labeling, have opened up new avenues for studying biochemical signaling down to the level of individual proteins—a project that will likely occupy cell biologists for the remainder of the century. However, with most currently available imaging systems, most protein transport and localized cellular events occur too rapidly for capture, particularly in three dimensions.

In this paper, we describe the construction and optimal operation of a high-speed, high-sensitivity, 3-D+time confocal system that has relatively modest cost and development time. This system can acquire 3-D images at near diffraction-limited resolution, with nearly single-photon sensitivity at the detector camera, and at frame rates up to 1000 fps. We also present sample results obtained using the system as built in our laboratory. Table 1 lists the major components of the microscope system and their approximate cost.

2 System Principles and Design

We present a diagram of our system in Fig. 1. In this section, we describe the options of various components, parameters of concern, caveats, integration issues, and choices made in our current system.

2.1 Confocal Spinning Disk

Background fluorescence arising from fluorescent labels or autofluorescent proteins outside of the focal plane presents a ubiquitous problem in fluorescence imaging. Confocal microscopy reduces this problem through the use of a pinhole—

both in illumination, by more tightly illuminating the focal plane, and in detection, by rejecting photons originating from outside the focal plane. The most common mode of confocal microscopy, laser scanning confocal microscopy (LSCM), achieves imaging by scanning a single illumination volume over the sample. (For a discussion of LSCM theory and signal to noise, see Ref. 4.) Yet the LSCM approach often does not yield the speed needed to visualize rapid dynamics.

Spinning disk confocal microscopy (SDCM), also called Nipkow disk microscopy, allows significantly greater imaging speeds by illuminating the sample at many separate spots simultaneously, through an array of pinholes on a disk, which rotates rapidly and scans the sample.[5–9] After passing back through the pinhole array, the emitted light projects onto a sensitive CCD detector. One exposure of the CCD takes the place of a complete scan of the field of view in LSCM. In the last several years, researchers have used SDCM to image a wide variety of subcellular dynamics (e.g., Refs. 5, 6, 10, and 11). Recent developments in SDCM, in particular the Yokogawa dual-spinning disk scan head equipped with a microlens array to raise illumination transmittance to 40%, have opened up the possibility of high-sensitivity three-dimensional imaging with unprecedented speed. In addition, the parallel imaging of SDCM means that for equivalent imaging speeds, SDCM requires less intense illumination than LSCM, which, in turn, can minimize nonlinear effects of photobleaching and phototoxicity.

Several commercially available models of SDCM units exist. Yokogawa produces the variable rotation speed CSU21 spinning disk confocal unit that we use. Their newer model, the CSU22, offers independent filter and dichroic control and has replaced the CSU21. Several companies, including Intelligent Imaging Innovations (3I), Solamere, and Perkin Elmer now sell Yokogawa units, often along with integrated software control and laser illumination. Other units have recently come

Address all correspondence to Ryan G. McAllister, Georgetown University, Department of Physics, Washington, DC 20057. Tel.: 202-687-6004; Fax: 202-687-2087; E-mail: rmca@physics.georgetown.edu
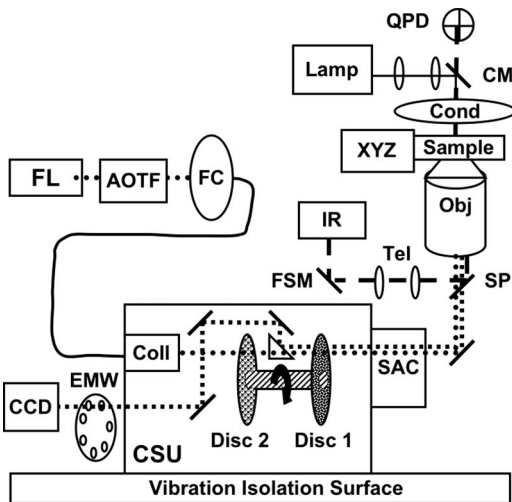
Fig. 1 A schematic of the setup as realized in our laboratory. Microscopy components: FL, fluorescent laser; AOTF, acousto-optic tunable filter; FC, fiber coupler; CCD, charge coupled device camera (including electron multiplied device(s)); CSU, confocal spinning disk unit (large box)); Coll, collimation optics inside the CSU; EMW, emission filter wheel; disk 1, microlens disk; disk 2 pinhole disk; SAC, spherical aberration correction device; Obj, objective; Sample, the imaging sample; XYZ, motorized XY stage and piezoelectric Z control; Cond, condenser; and Lamp, lamp for brightfield and DIC. In addition, the optical trap adds the following components: IR, infrared laser; FSM, fast steering mirror; Tel, telescope for magnification and creating conjugate planes; SP, short pass mirror; CM, cold mirror (replacing the microscope's standard metallic mirror); and QPD, quadrant photodiode.

to market at lower cost, but these also typically have significant limitations that reduce their utility for high-speed, high-resolution imaging.*

2.2 Spinning Disk Challenges and Limitations

The spinning disk confocal approach presents several challenges and limitations. Here we discuss the issues of synchronization, intensity fluctuations, a single pinhole size, and vibration.

Uniform exposure of the image requires synchronization of the camera and disk rotation with precision of a few microseconds; otherwise, some parts of the field of view receive a single pinhole pass more than other parts of the field of view. The image then will contain bright or dark arc-shaped streaks or dots aligned in arcs, depending on the amount of mismatch [see Fig. 2(a)]. For a given exposure mismatch, the relative contrast of this artifact increases for smaller number of passes per camera frame and thus appears more significant at faster imaging speeds. On the CSU21, serial port command or transistor-transistor logic (TTL) synchronization can select disk rotation rates up to 5000 rpm. This speed allows an imaging speed of up to 1000 fps because 1/12 of the disk provides complete coverage of the field of view. In our initial

---

*Programmable array microscope confocal (PAM) represents an alternative multi-illumination confocal approach to SDCM. PAM uses a micromirror array spatial light modulator to create the confocal effect.[12,13] The PAM approach can use custom illumination patterns and simultaneously collect the confocally rejected light and the confocal image. However, at this time we do not know of commercially available PAM confocal units.
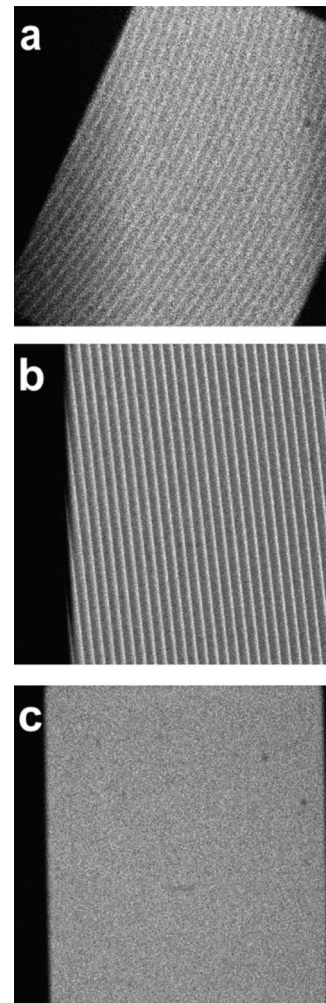
Fig. 2 Synchronization of spinning disk, illumination, and camera: (a) Exposure Mismatch: The appearance of the spinning disk artifact as arc-shaped streaks, caused by a camera exposure time not precisely synchronized with the spinning disk. (b) Frame transfer artifact: With good synchronization between camera exposure and disk speed, streaks still appear with a frame transfer camera, however these streaks appear as straight lines rather than arcs as in (a) (c) Artifacts eliminated: Elimination of both synchronization and frame transfer artifacts by accurate synchronization of disk speed and camera exposure time with illumination gated by camera exposure. Images of fluorescence reference slides (Microscopy Education) at 2-ms exposure time with electron multiplication gain using an Andor iXon 887 EM-CCD. Contrast adjusted in each image separately to maximize visibility of the artifacts.

SDCM implementation, Perkin Elmer (PE) SDCM Ultraview RS, the camera (ORCA AG, Hamamatsu) had an insufficiently accurate control of its exposure time that prevented precise synchronization between the camera exposure and the illumination.

In addition, frame transfer cameras, which includes most electron multiplied CCD cameras, can create another streaking artifact when used with a spinning disk. The camera pixels continue to accept photons during the vertical shift of the frame transfer for readout. In the time during which the frame transfer vertically shifts the pixels ($\sim 100~\mu$s), the spinning disk continues to move, generating linear streaks. Although
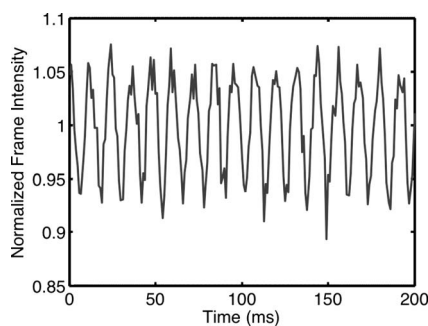
Fig. 3 Normalized frame intensity versus time for a fluorescent standard with AOTF-synchronized laser illumination showing intensity fluctuation due to asymmetries in the spinning disk unit. Exposure time corresponds to one-twelfth of a disk rotation (the shortest complete scan) at 5000 rpm. The intensity oscillates at the disk rotation rate. Images taken with a Cooke 1200 hs CMOS camera at 1000 fps with 1-ms exposure, and normalized by subtracting the darkfield intensity and dividing by the spatial mean. We also observe this intensity fluctuation with a photodiode at the microscope objective.

rotating the camera relative to the spinning disks can eliminate or significantly reduce these streaks, this has three disadvantages: cropping the field of view, camera orientation not matching ocular orientation, and confusing misalignment between sample motion and image motion. However, illuminating only during the camera exposure time (and thus not during the readout time) eliminates both streaking artifacts for any camera orientation. Most cameras have a TTL output that can trigger the illumination only during the exposure via the TTL input of the acousto-optic tunable filter (AOTF) driver.

SDCM does not provide perfectly even illumination within a disk rotation. Therefore, even with proper synchronization, spurious intensity fluctuations occur when imaging at exposure times that do not equal integer multiples of the disk rotation time. Figure 3 shows a time series of the normalized intensity of a fluorescent standard versus time, measured at 1000 fps. At all disk rotation rates, we observe an approximately sinusoidal oscillation with a frequency that matches the disk rotation rate. These fluctuations presumably result from misalignment or mechanical instability of the two spin-

ning disks, rather than to asymmetries of the disk itself, and their magnitude may vary between individual units of the same design.

Typically in LSCM, one adjusts the pinhole size to near the radius of the first Airy disk for a given objective and wavelength. The Yokogawa CSU models, however, do not support changeable disks and thus offer no way to adjust pinhole size. In practice, this does not usually present a significant limitation because the fixed 50 μm pinhole size optimally matches a common and convenient 100×1.4 NA objective. Furthermore, we have not observed degradation of resolution using 1.4 NA $60\times$ or other high-NA oil immersion objectives. For further comparison of optical performance between LCSM, SDCM, and widefield microscopy with deconvolution, see Ref. 14. Finally, the SDCM head introduces mechanical vibration into the imaging system (see Section 2.7).

2.3 Microscope

High-resolution imaging requires precise optical component positioning, making SDCM compatible generally with most high-end fluorescence microscopes. A microscope corrected for infinity space provides the advantage that placing flat optics in the infinity space region with minimal affect on image quality. Some microscopes offer a vertical stage extension option that expands the infinity space by a few inches. We used this extension to create space for inserting a laser line mirror for our optical trap into the microscope infinity space. (The same geometry also works for integration of a UV laser scalpel or photobleaching laser with appropriate changes to the added optics.) We chose a nonautomated, inverted, infinity microscope, the Nikon TE-2000 with vertical stage extension. We expect that with few adjustments one can build an equivalent apparatus on any other high quality infinity microscope.[†]

2.4 Camera

In contrast with LSCM, SDCM requires imaging with a camera. Note that, as described above, eliminating the confocal synchronization artifact requires a camera with highly precise exposure time control. The available cameras used for biological imaging include complementary metal oxide semiconductor (CMOS) cameras, charge-coupled device (CCD) cameras, electron multiplied CCDs (EMCCD), and cameras with image intensifiers. CMOS cameras offer high speed (often over 1000 full frames per second) but also high noise (often 80 e$^-$ rms read noise). High-end, cooled CCD cameras offer reduced noise at slow speeds (in the range of 10 full frames per second with 6 e$^-$ rms read noise). EMCCD cameras offer effectively lower noise (equivalent to 1 e$^-$ rms) compared to cooled CCDs and higher imaging speeds (around 30 full frames per second with pixel read rates in the range of $10-30$ MHz). Image intensifiers offer a high-gain addition to a camera in exchange for a loss of spatial resolution, at relatively high cost. In addition to noise considerations, the quan-

Table 1 Principal components.

Approximate cost ($1000)	Component
60–100	Confocal spinning disk unit (CSU)
20–60	Illumination laser
20–30	Electron multiplied charge couple device camera (EMCCD)
20–30	Microscope
20–30	Objectives
25–30	Motorized stage with piezoelectric z control
20	Software

[†]In outfitting our microscope for high-resolution DIC using an oil-immersion condenser and for sensitive force and position measurements using the optical trap, we discovered that the Nikon TE-2000 condenser system had significant mechanical play. This resulted in less reproducible positioning and a difficultly maintaining Köhler illumination. We found that replacing a thin (<1 mm thick) U-shaped piece of metal in the condenser mounting piece with a thicker 3-mm piece of aluminum considerably improved the stability and repeatability of the condenser alignment.

tum efficiency (QE) of a camera's pixels determines its effective sensitivity. Back-illuminated chips (for both CCDs and EMCCDs) have considerably higher QE than front-illuminated chips (~90% peak versus ~50% peak). In our system, we use the back-thinned EMCCD iXon DVM 887 (Andor). The newer DVM 888 offers more and slightly smaller pixels, but appears otherwise equivalent.

Dark current generally has such a low value in highly cooled CCDs and EMCCDs that it affects signal to noise only for acquisition times of >1 s per frame. However, the EM gain register amplifier increases the significance of clock-induced charge (CIC). CIC, also called spurious noise, refers to the small number of electrons impact ionized by the vertical shift voltage during the camera readout. CIC happens prior to the EM gain stage and occurs with Poisson statistics. By unequally amplifying photoelectrons, the EM gain also creates multiplicative noise on the signal, unless used in photon-counting mode. For a detailed discussion of CCD and EM-CCD issues, including noise, see Ref. 15.

EMCCDs generally use a frame transfer mode, which means that pixel exposure continues while frame reading occurs. This introduces two kinds of image artifacts: differential exposure (in both confocal and widefield) and streaking [spinning disk confocal only, see Fig. 2(c)]. As discussed above, in fluorescence imaging, using the AOTF to precisely synchronize the illumination with the camera exposure time eliminates both of these problems. In bright field, rotating the camera can eliminate the streaking artifact. Several technical note-style documents available from Andor's Web sites discuss these imaging artifacts and noise issues (see andor.com and emccd.com).

2.5 Laser

Although some spinning disk modules use or allow white light sources, LSCMs and the Yokogawa CSU only accept laser sources. Many prepackaged SDCM systems come with a standard laser illumination system with insufficient power for very high-speed imaging.

Ion gas lasers and, more recently, solid state lasers offer a range of visible wavelengths at useful powers. A gas laser can offer multiple wavelengths (in the case of argon/krypton mixed gas lasers, typically useable lines include 488, 514, 568, and 647 nm light); however, these lasers rely on plasma tubes with limited lifetimes, require maintenance of alignment, and typically require forced-air or water cooling. Currently, gas lasers can provide more light than solid state lasers in the visible wavelength with some notable exceptions; for example, frequency-doubled yattrium iron garnet lasers can provide high power at 532 nm green.

Adding a custom gas laser (such as from Laser Innovations or Coherent) requires performing the AOTF alignment and fiber coupling, as described in Ref. 5. Gas lasers require more cleaning of optics, regular realignment, and every few years, plasma tube replacement.

Among solid state lasers, fiber-coupled visible diode lasers (such as those from Point-Source) offer greater reliability and stability, though lower power, than gas lasers. Fiber-coupling a diode laser involves greater complexity, due to the high astigmatism and otherwise poor beam quality of diode lasers.

Fortunately commercial vendors sell many precoupled designs.

2.6 Piezo z Control

Either a piezoelectric objective positioner or a piezoelectric z-axis top plate integrated into the xy stage can achieve the fast, precise control of focal plane z position required for high-quality 3-D imaging. We have found that a piezoelectric z-axis top plate has three advantages over an objective positioner: (i) better differential interference contrast (DIC) image quality, (ii) better parfocality and paraxiality between objectives, and (iii) changing z focus depth does not change the distance between the condenser and the objective, and thus more closely maintains Köhler illumination, even while changing focal planes. The piezo-objective positioner can degrade image quality and parfocality/paraxiality by introducing extra space between the objective turret and the objective and, at least in the case of our objective piezopositioner (Piezosystems Jena), by placing the objective off center by ~0.5 mm. While transitioning to a piezo-z top plate (Applied Scientific Instruments), we found it easy to change from one to the other because both respond to a 0–10 V signal control signal, generated either by an IO board (National Instruments) or by the z output on the synchronization box from our original PE system.

The choice of camera and z motion control/synchronization can significantly impact imaging speed. The top speed of the ASI piezo top plate (5 mm/s) can acquire z stacks using the full speed of the SDCM. However, the serial port control normally used by imaging integration software severely limits positioning speed. On the other hand, Slide-Book (3I) offers an optional hardware package that allows for analog control of the plate, and we have driven z acquisition at ~25 ms per z step. In this case, the software synchronization between camera and z stage limits the acquisition rate. With a second optional package that uses hardware synchronization for capture, we have demonstrated that SlideBook can drive the ASI z top plate much faster: at ~6 ms per z step with a Cascade II camera. In this case, the camera's frame rate rather than either the piezospeed or the software/hardware control limited the acquisition rate; thus, faster cameras could presumably acquire even faster z stacks. The high scanning speeds did not produce observable increases in distortions in the xz projections of fluorescent microspheres.

2.7 Vibration Isolation

We place the entire apparatus on a Newport optical table with XL-A pneumatic vibration isolation legs (Newport has several newer options) to increase the long-term stability of component alignment and reduce the potential for vibration-induced blur and focus drift during imaging. However, the vibration isolation table does not protect against disturbances generated either (i) at low frequency (below a few Hertz) or (ii) by devices also on or mechanically coupled to the table. To reduce vibration, we remove as many electronic components from the table as possible, placing them on a hanging shelf above the table or on the floor below.

Because of the spinning disks, the SDCM itself causes vibrational noise at the microscope stage, as seen in accelerometer measurements and in the position signal from a bead

trapped in the laser tweezer [measured with the quadrant pizoto diode (QPD)]. Power spectra of both signals show slight peaks at the disk speed and its harmonics, and a stronger, broader peak around $1-2$ kHz. The kilohertz vibrations grow in amplitude with increasing spinning disk speed. At the fastest disk rotation rate (5000 rpm), we estimate an rms vibration amplitude of ~10 nm at the stage. Because the vibration amplitude represents a displacement over an order of magnitude smaller than our point-spread function, we consider the vibrations' effect on image quality negligible. QPD force measurements have high sensitivity to vibration, however. When calibrating our optical trap using the power spectrum method, we have found only negligible vibrations at a moderate spinning disk rotation speed (1667 rpm, corresponding to a maximum 333 fps imaging speed).

2.8 Integrating IR Optical Trap

We chose a 2 W YLM ytterbium-doped fiber ring laser (IPG Photonics) with an internal diffraction grating that tunes the wavelength to 1064 nm. This inexpensive option for a 2 W IR laser provides a well-collimated Gaussian beam ($M^2 < 1.05$) and the convenience of a common wavelength already matched to inexpensive laser optics. Even at this long wavelength, we can image the reflection of the optical trap off of the coverslip or other glass surface, allowing us to observe beam position and quality. However, only the long pass dichroic and emission filter pair in our CSU 21 allow us to view the beam with little distortion.

The short pass (SP) dichroic (Omega Optical, SP in Fig. 1) inserted into the microscope's optical path has finite thickness (~1 mm) and lies at a 45-deg angle to the optical axis of the microscope. Therefore, the dichroic displaces the optical axis of the microscope relative to the objective's optical axis. The thicker the optic, the larger this displacement and, thus, the larger the resulting degradation in image quality.

2.9 Other Components

A fast, external filter wheel adds flexibility to the Yokogawa scan heads and decreases the time required to switch emission filters in multichannel imaging. The addition of a filter wheel involves finding a model with a matching adaptor, such as the Lambda series (Sutter), and choosing a field lens, which determines both magnification and camera position for parfocality with the eyepiece. We use a micrometer slide or high-resolution imaging target (both available from Edmund's Industrial Optics) to determine actual magnification.

Supplied by the manufacturer of the microscope, DIC optics (two polarizers and two waveplates) provide an additional imaging modality that essentially converts index of refraction gradients into contrast. We mounted an additional polarizer in the automated emission filter wheel and carefully oriented it to match the one provided by Nikon as the DIC analyzer. This allows us to use the automated emission filter wheel for fast switching between DIC and fluorescence.

2.10 System Control and Software

When choosing software control, we had to consider what software could control the essential components, the confocal, piezo z control, AOTF, and camera, in a fashion useful for high-speed imaging. The SlideBook software suite, from 3I can control all of the hardware described above with the exception of the IR optical trap.

3 Optimizing Image Quality and Correcting Image Aberrations

Several optical phenomena will result in an image not accurately representing the relative locations of the light sources in the sample. Unfortunately, microscope manufacturers provide too little information about their optics for calculation of these aberrations. Even without this information, we can describe, measure, and sometimes even correct for these aberrations, for example, by using polynomial models presented in ray optics texts, such as Ref. 16.

The difference in index of refraction between the mounting medium and the immersion medium causes the distance the objective moves to differ from the distance the image plane moves in the z direction. In the case of an oil immersion objective ($n_i = 1.515$) and a waterlike mounting medium ($n_s = 1.33$), this results in an apparent stretching of the z size of acquired voxels, which we remove in postprocessing by multiplying the z length scale by the ratio (0.88). In this system, we have also found two removable sources of coma: the objective piezoelectric z stage and the imprecision in the mechanical location of the objective turret on the Nikon TE 2000 microscope. As mentioned, we have therefore replaced the objective piezoelectric z focus with a piezoelectric z stage (ASI) and carefully aligned the objective turret mount.

3.1 Spherical Aberration

Typical high-NA oil immersion objectives have correction for spherical aberration but only at a small, fixed distance beyond the coverslip. Some objectives have a correction collar that allows for manual reduction of spherical aberration, but this correction remains static during acquisition of z stacks.

3I has developed a spherical aberration correction [(SAC) also called InFocus] device compatible with the Yokogawa confocal head. Inserted between the microscope body and the confocal head and controlled by the 3I software, the SAC can correct for spherical aberration as a function of focal plane depth within a given sample. Because spherical aberration varies with imaging depth, this "rolling" correction minimizes spherical aberration more effectively than an objective correction collar or other static correction.

To test the SAC unit with our confocal, we prepared 1.0-μm green (508 nm) fluorescent beads (Duke Scientific Corp., Part No. G0100) in a 0.2% type I collagen gel, as described in Ref. 17. Figure 4 presents a plot of the maximum intensity projection as a function of depth for beads in collagen imaged with 488-nm excitation and the 500-nm long-pass dichroic in the CSU 21 confocal head. Fitting an xz maximum intensity projection of a bead to a 2-D Gaussian, we observe about a 20% reduction in z size of the beads with the SAC as compared to without the SAC. In both cases, the z size of the bead images increases with depth. The SAC has the more dramatic effect of increasing the relative bead image intensity deep in the sample. Without the SAC, the brightness of bead images drops off significantly with depth in the collagen; whereas with the SAC, the brightness of beads drops of much less steeply (see Fig. 4). Spherical aberration degrades
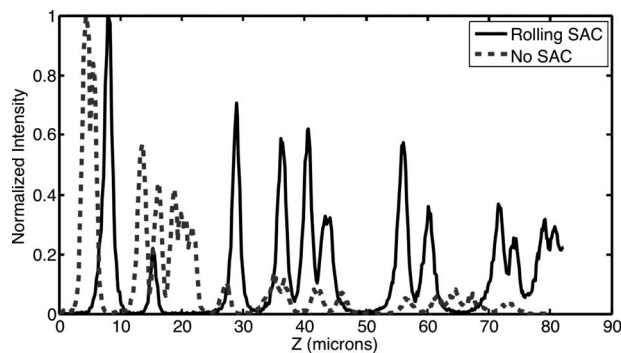
Fig. 4 Comparison of images of 1.0-μm fluorescent beads in a 0.2% collagen gel with and without SAC. Curves represent maximum voxel intensity in each z plane. Note that intensity of beads imaged with the rolling SAC (solid curve) decreases much less steeply than the intensity of the beads imaged without the SAC (dashed curve). Gaussian fits of the beads profile along Z show that in both cases, bead images expand considerably with depth. SAC results in about a 20% reduction in width along Z anywhere beyond the first 10 μm. Intensity normalized by subtracting the minimum and then dividing by the maximum for each curve. Images acquired with 488 nm excitation, and with DF immersion oil (Cargille) to reduce background fluorescence.

both the intensity of the illumination and the fraction of emitted light that passes through the pinholes to reach the detector.

4 Results

As an example application of this system, we have extended fluorescence correlation spectroscopy (FCS) to SDCM (spinning disk FCS), which allowed us to produce spatial maps of diffusion times in complex environments. Figure 5 shows a spinning disk FCS measurement of mean diffusive residence times of fluorescent microspheres diffusing in collagen. The spatial structure of the collagen causes the spatial structure in the residence times.
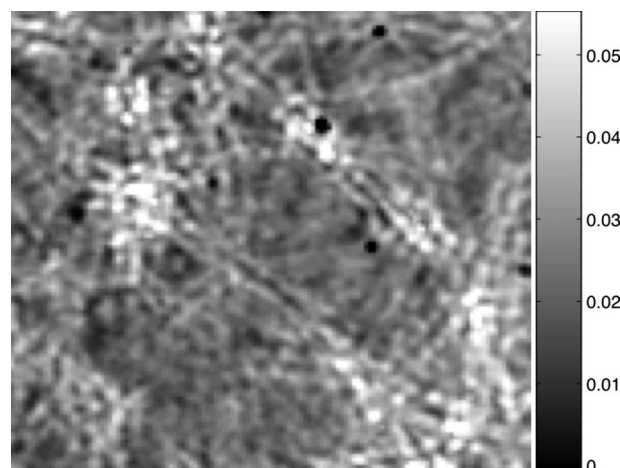

Fig. 5 Map of mean diffusive residence time in seconds of fluorescent microspheres in collagen measured by spinning disk FCS. The spatial variation originates from the collagen fibrils that alter the spheres diffusive motions through steric and hydrodynamic interactions. The collagen concentration of 2 mg/ml gives a mean pore size of ~1 μm, and the spheres had a diameter of 210 nm. See Ref. 17 for details.
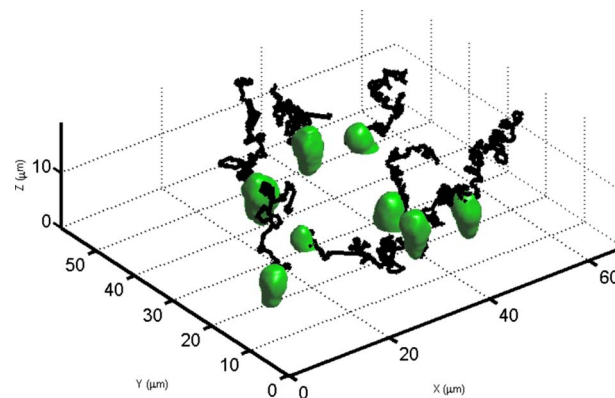
Fig. 6 Each green isosurface represents a 1-μm sphere diffusing in a 95% glycerine 5% water solution. Each black trace represents the paths a bead center of intensity followed during a 298 time point section of a longer acquisition. The acquisition took place with 1.7 s between time points, with each time point consisting of 40 z planes, each exposed for 20 ms with 40 ms between z planes. (Color online only.)

We have also used this system to track diffusion of particles in three dimensions. Figure 6 shows the paths taken by 1-μm fluorescent spheres diffusing through a solution of 95% glycerine and 5% water. The green isosurfaces show the bead positions in the first stack of the series. The black curves show the bead paths during the 4-D acquisition determined by particle tracking. Each of the 298 3-D stacks consist of 40 z slices taken at 20 ms exposure, with 40 ms between z positions, and ~1.7 s between stacks. Each stack occupies a total of 20 μm in the z direction, with a z spacing of 500 nm.

In living cells, we have imaged quickly moving fluorescent speckles. Figure 7 shows three frames from a 3-D+time
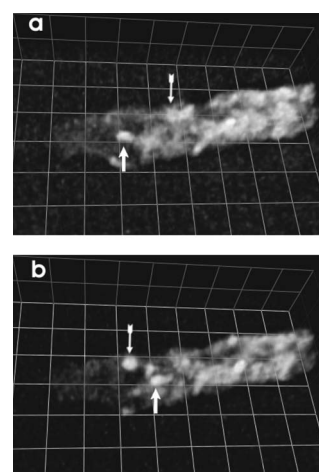
Fig. 7 Two frames from a 3-D + time movie of fluorescent eb3-eGFP, a microtubule associated protein, in an axon-like protrusion from a living cell. To allow for feature visibility in the figure, we present a small section of the imaged neurite. The fluorescent eb3 creates speckles that move quickly within the neurite. The imaging speed of this system (100 ms/z slice, 1.1 s per z stack) allows resolution of these features. Arrows highlight two eb3 speckles in each frame, at different z depths, one emerging from and one headed into the denser region of the neurite. Frame (b) follows three frames, or 3.3 s, after frame (a).

movie of a neurite from a differentiated PC12 cell. Fluorescently labeled eb3, which binds to the plus end of growing microtubules, results in the moving speckles, which we can resolve with the described instrument. In a conventional LSCM, live-cell imaging with the requisite sensitivity typically requires scans of ∼1 s per z slice or slower. At these acquisition speeds, the speckle images would have too much blur for recognition. In addition, we have used the imaging system described above to produce novel results with live red blood cells infected with malarial parasites.[18,19]

5 Conclusion

We have described how to build a customized, high-speed confocal imaging system at relatively low cost using a spinning-disk confocal microscope. In the absence of camera-imposed limitations, this system can image 2-D or 3-D samples at up to 1000 fps at close to the diffraction limit of optical resolution. With improvements in fluorescent labeling and camera and laser technology, we expect the capabilities of this approach to expand in the near future.

References

1. K. W. Eliceiri and C. Rueden, "Tools for visualizing multidimensional images from living specimens," *Photochem. Photobiol.* **81**, 1116–1122 (2005).
2. D. J. Stephens and V. J. Allan, "Light microscopy techniques for live cell imaging," *Science* **300**, 82–86 (2003).
3. C. J. Weijer, "Visualizing signals in moving cells," *Science* **300**, 96–100 (2003).
4. J.-A. Conchello and J. W. Lichtman, "Optical sectioning microscopy," *Nat. Methods* **2**, 920–931 (2005).
5. M. C. Adams, W. C. Salmon, S. L. Gupton, C. S. Cohan, T. Wittmann, N. Prigozhina, and C. M. Waterman-Storer, "A high-speed multispectral spinning-disk confocal microscope system for fluorescent speckle microscopy of living cells," *Methods* **29**, 29–41 (2003).
6. P. S. Maddux, B. Moree, J. C. Canman, and E. D. Salmon, "Spinning disk confocal microscope system for rapid high-resolution, multimode, fluorescence speckle microscopy and green fluorescent protein imaging in living cells," *Methods Enzymol.* **360**, 597–617 (2003).
7. T. Tanaami, S. Otsuki, N. Tomosada, Y. Kosugi, M. Shimuzu, and I. Ishida, "High speed 1-frame/ms scanning confocal microscope with a microlens and Nipkow disks," *Appl. Opt.* **41**, 4704–4708 (2002).
8. A. Egner, V. Andresen, and S. W. Hell, "Comparison of the axial resolution of practical Nipkow-disk confocal fluorescence microscopy with that of multifocal multiphoton microscopy: Theory and experiment," *J. Microsc.* **206**, 24–32 (2001).
9. S. Inoué and T. Inoué, "Direct-view high-speed confocal scanner—The CSU-10," in *Cell Biological Applications of Confocal Microscopy*, 2nd ed., Academic Press, New York (2000).
10. V. V. Artym, Y. Zhang, F. Seillier-Moiseiwitsch, K. M. Yamada, and S. Mueller, "Dynamic interactions of cortactin and membrane type 1 matrix metalloproteinase at invadopodia: Defining the stages of invadopodia formation and function," *Cancer Res.* **66**, 3034–3043 (2006).
11. W. C. Salmon, M. C. Adams, and C. M. Waterman-Storer, "Dual-wavelength fluorescent speckle microscopy reveals coupling of microtubule and actin movements in migrating cells," *J. Cell Biol.* **158**, 31–37 (2002).
12. P. J. Verveer, Q. S. Hanley, P. W. Verbeek, L. J. van Vliet, and T. M. Jovin, "Theory of confocal fluorescence imaging in the programmable array microscope (PAM)," *J. Microsc.* **189**, 192–198 (1998).
13. Q. S. Hanley, P. J. Verveer, M. J. Gemkow, D. Arndt-Jovin, and T. M. Jovin, "An optical sectioning programmable array microscope implemented with a digital micromirror device," *J. Microsc.* **196**, 317–331 (1999).
14. J. M. Murray, P. L. Appleton, J. R. Swedlow, and J. C. Waters, "Evaluating performance in three-dimensional fluorescence microscopy," *J. Microsc.* **228**, 390–405 (2007).
15. J. B. Pawley, Ed., *Handbook of Biological Confocal Microscophy*, pp. 918–931, Springer, New York (2006).
16. V. N. Mahajan, *Optical Imaging Aberrations*, SPIE, Bellingham, WA (1998).
17. D. R. Sisan, R. Arevalo, C. Graves, R. McAllister, and J. S. Urbach, "Spatially resolved fluorescence correlation spectroscopy using a spinning disk confocal microscope," *Biophys. J.* **91**, 4241–4252 (2006).
18. B. Gligoreijevic, T. Bennett, R. McAllister, J. Urbach, and P. D. Roepe, "Spinning disk confocal microscopy of intraerythrotic malarial parasites II: Altered vacuolar volume regulation in drug resistant malaria," *Biochemistry* **45**, 12411–12423 (2006).
19. B. Gligoreijevic, R. McAllister, J. Urbach, and P. D. Roepe, "Spinning disk confocal microscopy of intraerythrotic malarial parasites I: Quantification of hemozoin development," *Biochemistry* **45**, 12400–12410 (2006).